REPORT DOCUMENTATION PAGE

AFRL-SR-BL-TR-02-

0104

1. REPORT DATE (DD-MM-YYYY)	2. REPORT TYPE	3. DATES COVERED (From - To)
28-02-2002	Final Report 2001	02/01/98-01/31/01

4. TITLE AND SUBTITLE
Ceramic Nanocrystals

5a. CONTRACT NUMBER

5b. GRANT NUMBER
F49620-98-1-0243

5c. PROGRAM ELEMENT NUMBER

6. AUTHOR(S)
A. Paul Alivisatos

5d. PROJECT NUMBER
2303/EX

5e. TASK NUMBER

5f. WORK UNIT NUMBER

7. PERFORMING ORGANIZATION NAME(S) AND ADDRESS(ES)
University of California, Berkeley
Department of Chemistry
B 62 Hildebrand Hall
Berkeley, CA 94720-1460

8. PERFORMING ORGANIZATION REPORT NUMBER

9. SPONSORING / MONITORING AGENCY NAME(S) AND ADDRESS(ES)
AFOSR/NL
801 N Randolph St Suite 732
Arlington VA 22203-1977

10. SPONSOR/MONITOR'S ACRONYM(S)
AFOSR/NL

11. SPONSOR/MONITOR'S REPORT NUMBER(S)

12. DISTRIBUTION / AVAILABILITY STATEMENT

DISTRIBUTION STATEMENT A
Approved for Public Release
Distribution Unlimited

20020401 010

13. SUPPLEMENTARY NOTES

14. ABSTRACT

We have shown that it is possible to prepare disposable nanocrystals of transition metal oxides in the absence of water or air by thermal decomposition of metal Cupferron complexes in hot surfactants. Preliminary experiments suggest that a similar level of size control as in the synthesis of semiconductor nanocrystals is possible. Since the precursor is available for many metal elements, this approach may present a rather general route to metal oxide nanocrystals. In another study resonant photoemission electron microscopy (PEEM) at the FeL absorption edge was utilized to image single gamma-Fe2O3 nanocrystals of 10 nm average diameter (approximately 20,000 Fe atoms) and to record soft x-ray absorption spectra of individual particles. Within the spectral resolution of the experiment, no damage to the individual nanoparticles occurs during repeated prolonged exposures to the intense x-ray beam. Furthermore, no differences in the x-ray absorption spectrum of a single nanocrystal are observed whereas PEEM contrast images and absorption spectra show strong intensity variations. This proof-of-principle experiment demonstrates the applicability of x-ray spectromicroscopy to the study of nanoscale systems on a hitherto unachieved length scale.

15. SUBJECT TERMS
Nanocrystals, soft x-ray imaging, spectroscopy

16. SECURITY CLASSIFICATION OF:			17. LIMITATION OF ABSTRACT	18. NUMBER OF PAGES	19a. NAME OF RESPONSIBLE PERSON
a. REPORT	b. ABSTRACT	c. THIS PAGE			A. Paul Alivisatos
Unclassified	Unclassified	Unclassified			19b. TELEPHONE NUMBER (include area code) 510-643-7371

Final Report 2001
Ceramic Nanocrystals
AFOSR Grant No. F49620-98-1-0243

A. Paul Alivisatos
Chancellor's Professor of Chemistry and
Materials Science
Department of Chemistry
University of California, Berkeley
Berkeley, California 94720-1460

T 510 643 7371
F 510 642 6911
Email: alivis@uclink4.berkeley.edu

Accomplishments:

- Developed a new synthetic procedure for metal oxide nanocrystals
- Performed x-ray absorption spectroscopy on single metal oxide nanocrystals
- Work on pressure and temperature-induced structural transofrmation sin metal oxide nanocrystals is on-going

Comprehensive Technical Summary:

Due to the interesting size-dependent properties of nanocrystals, their preparation by colloidal methods has gained considerable interest in recent years.(1,2) Especially for semiconductor and metal nanocrystals, the injection of molecular precursors into hot coordinating solvents at high temperatures has achieved a very sophisticated level yielding samples with good size control, narrow size distributions and good crystallinity of individual and soluble nanocrystals.(3-5) In contrast, the synthesis of nanocrystalline transition metal oxides relies mainly on hydrolytic, hydrothermal or sol-gel preparations, which only rarely yield similar high-quality samples. However, due to the interesting physical and chemical properties of transition metal oxides like superconductivity, colossal magnetoresistance, metal-insulator transitions as well as their wide-spread use in catalysis, ceramics, energy storage, magnetic data storage, sensors etc., they represent a very interesting field for nanocrystal research.

In addition, the synthesis of metal oxide nanocrystals by non-hydrolytic methods is by itself a very interesting task since it yields nanocrystals with non-hydroxylated surfaces. In consequence, their properties should be markedly different from nanocrystals prepared by hydrolytic methods. For instance, it was shown very recently that removing hydroxyl groups from hydrated oxide gels via a silanization step profoundly limits the crystal growth in the subsequent high-temperature calcination of the gel.(6) So far, only one paper has been published which described the direct solution-based synthesis of non-hydroxylated, individual TiO2 nanocrystals.(7) We report here a new non-hydrolytic single-precursor approach to the synthesis of soluble nanocrystals of transition metal oxides, which utilizes some concepts of the preparation of semiconductor nanocrystals. A promising molecular precursor for transition metal oxide nanocrystals are metal cupferron complexes MxCupx (M: metal ion; Cup: Cupferron or N-nitroso-N-hydroxyl-phenylamine) which are used in the precipitation or extraction of metal ions from aqueous solution.(8) They are easily prepared for many metal elements and decompose to the respective oxides around 200 °C in N2. We show in the following, that injecting a solution of metal cupferron complexes in octylamine into long-chain amines at 250 - 300 °C yields nanocrystals of iron oxide, manganese oxide and copper oxide. These nanocrystals are 4 - 10 nm in size, single-crystalline and soluble in organic solvents. As cupferron complexes are available for almost all metal elements, the use of this precursor might offer an interesting general approach to metal oxide nanocrystals. The preparation of the metal cupferron complexes is based on the precipitation of metal ions from aqueous solution at a specific pH with the respective ammonium salt of cupferron. In all three cases, the elemental analysis and the powder x-ray diffraction (XRD) patterns agreed well with single-crystal data.(9-11) Also, FT-IR spectroscopy excluded the presence of excess ammonium cupferron, water or solvent molecules and agreed well with results given in ref. 12.

Heating of these dried powders in a DTA / TGA apparatus under N2 show sharp decomposition temperatures at 180 °C, 230 °C and 205 °C for FeCup3, MnCup2 and CuCup2, respectively. XRD of the respective decomposition products reveal that they consist of g-Fe2O3, MnO and Cu. The latter is a consequence of the reduction of CuO/Cu2O at high temperatures under inert atmosphere. This result proves thereby that metal cupferron complexes can indeed act as molecular precursor for transition metal oxides in the absence of O2 and H2O.

An important feature of the synthesis of semiconductor nanocrystals is the injection of molecular precursors into hot surfactants. The idea is to initiate crystal nucleation at high temperatures and controlling the growth by lowering the reflux temperature and coordinating surfactants to the surface of the nanocrystal. The same principle was used for the synthesis of transition metal oxide nanocrystals. In the following, a typical synthesis yielding iron oxide nanocrystals with 6 - 7 nm particle sizes is described. To remove oxygen and water, 7 g of trioctylamine was heated to 100 °C for 1 - 1.5 h and repeatedly evacuated to 20 mtorr and purged with Ar. A solution of 0.3 M FeCup3 in octylamine was treated the same way at 60 °C. Then, 4 ml of FeCup3 stock solution were rapidly injected at 300 °C under vigorous stirring and Ar atmosphere. A color change of the solution from colorless to dark-brown and a strong gas evolution indicated the decomposition of the cupferron complex. After refluxing for 30 min. at 225 °C, the heating was stopped. At room temperature the flask contained a dark-brown, clear liquid supernatant and a black precipitate, which were separated by centrifugation. Adding organic solvents like toluene, HCl3 etc. to this precipitate yielded clear deep-brown stable solutions which contain nanocrystals of iron oxides and which could be precipitated again by addition of methanol. Adding methanol to the supernatant of the reaction leads to a brown precipitate, which also could be dissolved and reprecipitated by suitable solvents. For both fractions, dissolution and reprecipitation could be repeated several times.

Similar procedures have been used in the synthesis of manganese oxide and copper oxide nanocrystals. In case of manganese oxide, an orange precipitate was obtained after the reaction, which dissolved in toluene, accompanied by a color change from orange to brown. In case of CuCup2, a primary amine (e.g. hexadecylamine) has to be used as surfactant to disperse the precipitated nanocrystalline copper oxide in toluene or CHCl3. In addition, the reaction has to be stopped immediately after reaction since the formation of metallic Cu instead of the copper oxide is favored at high temperatures under Ar atmosphere.

We have shown that it is possible to prepare soluble nanocrystals of transition metal oxides in the absence of water or air by thermal decomposition of metal cupferron complexes. Preliminary experiments suggest that a similar level of size-control as in the synthesis of semiconductor nanocrystals is possible. Since the precursor is available for many metal elements, this approach might present a rather general route to metal oxide nanocrystals. It can be expected that this synthesis route enables manipulations of transition metal oxide nanocrystals which are similar to the ones achieved with semiconductor and metal nanocrystals like incorporation into optical, electronic and photovoltaic devices,(20-23) and the linkage to DNA and biomolecules.(24-26)

(1) Alivisatos, A. P. Science 1996, 271, 933-937.
(2) Heath, J. M. Acc. of Chem. Res. - Nanoscale Materials Special Issue, 1999; Vol. 32.
(3) Murray, C. B.; Norris, D. J.; Bawendi, M. G. J. Am. Chem. Soc. 1993, 115, 8706-8715.
(4) Peng, X.; Wickham, J.; Alivisatos, A. P. J. Am. Chem. Soc. 1998, 120, 5343-5344.
(5) Sun, S.; Murray, C. J. Appl. Phys. 1999, 85, 4325-4330.
(6) Wu, N.-L.; Wang, S.-Y.; Rusakova, I. A. Science 1999, 285, 1375-1377.
(7) Trentler, T. J.; Denler, T. E.; Bertone, J. F.; Agrawal, A.; Colvin, V. L. J. Am. Chem. Soc. 1999, 121, 1613-1614.
(8) Comprehensive coordination chemistry: the synthesis, reactions, properties & applications of coordination compounds; 1st ed.; Pergamon Press: Oxford, England, 1987; Vol. 2, Chapt. 15.9.2.
(9) Helm, D. v. d.; Merritt, L. L.; Degeilh, R.; MacGillavry, C. H. Acta Cryst. 1965, 18, 355-362.
(10) Elerman, Y.; Atakol, O.; Svoboda, I.; Geselle, M. Acta Cryst. C 1995, 51, 1520-1522.
(11) Tamaki, K.; Okabe, N. Acta Cryst. C 1996, 52, 1612-1614.
(12) Kellner, R.; Prokopowski, P. Analytica Chimica Acta 1976, 86, 175-184.
(13) Kraus, W.; Nolze, G. J. Appl. Cryst. 1996, 29, 301-303.
(14) Shmakov, A. N.; Kryukova, G. N.; Tsybulya, S. V.; Chuvilin, A. L.; Solovyeva, L. P. J. Appl. Cryst. 1995, 28, 141.
(15) Jarosch, D. Mineral. Petrol. 1987, 37, 15-23.
(16) Neuburger, M. C. Z. Phys. 1930, 67, 845-850.
(17) Cullity, B. D. Elements of X-ray Diffraction; 2nd ed.; Addison-Wesley: Reading, MA, 1978.
(18) Murray, C. B.; Kagan, C. R.; Bawendi, M. G. Science 1995, 270, 1335-1338.
(19) Chemseddine, A.; Weller, H. Ber. Bunsenges Phys. Chem. 1993, 97, 636-637.
(20) Colvin, V. L.; Schlamp, M. C.; Alivisatos, A. P. Nature 1994, 370, 354-357.
(21) Mattoussi, H.; Radzilowski, L. H.; Dabbousi, B. O.; Thomas, E. L.; Bawendi, M. G.; Rubner, M. F. J. Appl. Phys. 1998, 83, 7965-7974.
(22) Klein, D. L.; Roth, R.; Lim, A. K. L.; Alivisatos, A. P.; McEuen, P. L. Nature 1997, 389, 699.
(23) Huynh, W. U.; Peng, X.; Alivisatos, A. P. Adv. Mater. 1999, 11, 923-927.
(24) Alivisatos, A. P.; Johnsson, K. P.; Peng, X. G.; Wilson, T. E.; Loweth, C. J.; Bruchez, M. P.; Schultz, P. G. Nature 1996, 382, 609-611.
(25) Bruchez, M.; Moronne, M.; Gin, P.; Weiss, S.; Alivisatos, A. P. Science 1998, 281, 2013.
(26) Storhoff, J.; Mirkin, C. Chem. Rev. 1999, 99, 1849-1862.

X-ray absorption spectroscopy of single transition metal oxide nanocrystals

The fabrication and manipulation of solid-state nanoscale structures has attracted considerable interest in recent years due to its promise of enabling new technologies in areas ranging from information processing and storage, optics and telecommunication, power generation and energy storage to medicine and biology.(1,2) In particular, the bottom-up approach using wet-chemical methods to prepare soluble nanocrystals of inorganic materials

with sizes ranging from about 1 nm to 20 nm holds great promise to provide the necessary nanoscale building blocks. However, although tremendous progress has been achieved in recent years in the synthesis and self-assembly of surfactant-capped nanocrystals of semiconductors and metals,(3-10) even the currently best procedures yield samples with distributions with respect to particle size and shape as well as crystallinity and defect structure. In the case of multi-component systems like semiconductor and metal core-shell nanoparticles or metal alloy nanocrystals, the additional complication exists that the particles might not be of uniform chemical composition.

In consequence, scaling laws derived from experiments on such particle ensembles exhibit an inherent uncertainty with respect to intrinsic properties of individual nanoparticles. This makes it highly desirable to use techniques that can yield information about the properties of individual particles. Most recent developments in this respect include the measurement of the optical fluorescence of single semiconductor nanocrystals,(11,12) Raman spectroscopy of individual carbon nanotubes,(13,14) scanning tunneling microscopy and spectroscopy as well as scanning probe microscopy of a wide range of different nanostructures.(15-17) Especially, transmission electron microscopy (TEM), particularly in high-resolution mode, has been used extensively and successfully for many years to obtain information about the size, the shape, the crystallinity, and, to some extent, the elemental composition of individual particles.(18-21) In addition, the use of spatially resolved electron energy loss spectroscopy (EELS) allows one to determine the elemental composition as well as the oxidation state on a nanometer length-scale.(22,23) Recent studies also illustrated the capability of atomic contrast scanning TEM imaging and EELS spectroscopy to study the elemental composition and surface structure of individual CdSe nanocrystals on a sub-nanometer length scale.24 Finally, Lorentz-microscopy in TEM allows investigation of the magnetization direction of individual nanocrystals.(25) Another very powerful technique for the study of nanostructured materials is core-level x-ray spectroscopy, since detailed information about the local structure can be obtained even in the absence of structural long-range order in the sample. In addition, the unique sensitivity of x-ray spectroscopy to a wide range of material properties like elemental composition, electronic and crystallographic structure, and sensitivity to orientation phenomena due to structural or magnetic ordering makes it particularly attractive.(26,27) Consequently, x-ray absorption spectroscopy has extensively been used to characterize ensembles of colloidal nanocrystals with sizes ranging from 1 - 10 nm.(28-31) However, similar to other ensemble spectroscopy techniques the interpretation of the data is impaired by the fact that even the best colloidal samples to date are not mono-disperse with respect to particle size and shape. Therefore, the development of single particle x-ray spectroscopy techniques is highly desirable.

X-ray spectromicroscopy is a combined imaging and spectroscopy technique for the characterization of samples on a sub-micron length scale utilizing x-ray absorption or x-ray photoemission spectroscopy.(32-35) So far, to the best of our knowledge only the measurement of spatially resolved x-ray photoemission and low-energy electron spectra of InAs quantum dots with a mean diameter and height of 53 nm and 22 nm, respectively, grown by the Stranski-Krastanov growth mode, has been reported.(36,37) Here, we demonstrate the application of spatially resolved Photoemission Electron Microscopy (PEEM) to measure soft x-ray absorption spectra at the Fe L3,2 edges of single colloidal iron oxide nanocrystals with an average diameter of 10 nm (~ 20,000 iron atoms).

Surfactant-capped nanocrystals of g-Fe2O3 (maghemite) were prepared by a slightly modified version of a recently published procedure using hexadecylamine as surfactant.(38) Two milliliters of a 0.3 M solution of iron cupferronate in octylamine was injected into 5 g of hexadecylamine at 300 °C. After injection, the reaction mixture was heated for 60 min. at 270 °C and subsequently cooled to 100 °C. The reaction mixture was transferred into a 2 - 3 fold excess of methanol and the resulting precipitate of surfactant-capped nanocrystals was redispersed in toluene. A fraction was isolated by repeated size-selective precipitation using methanol as precipitating agent and the average particle size was determined by TEM to be 10 nm with a standard deviation of 3 nm. Very dilute toluene solutions of this sample were spin-coated onto silicon wafers that were freshly cleaned by etching with HF and washing with deionized H2O. The particle coverage of the silicon substrate was determined by high-resolution Scanning Electron Microscopy (SEM) at the National Center for Electron Microscopy, Lawrence Berkeley National Laboratory, Berkeley, operating at 5 kV with a sample current of 12 mA.

The PEEM experiments were performed at the bending magnet beamline 7.3.1.1 of the Advanced Light Source (ALS), Berkeley.39 X-rays with linear or circular polarization illuminate the sample under a 30° incident angle forming an approximately 30 mm wide stripe. The low-energy secondary photoelectrons generated by the absorption of x-rays are accelerated into the electron microscope column by a voltage of typically 20 kV applied between the sample and the first grounded objective lens (distance of about 2 mm). The electrons are directed and magnified onto a phosphor screen that is digitized by a CCD. Image contrast can arise from a number of mechanisms including topographical, elemental, and chemical inhomogeneities in the sample. In addition, structural and magnetic domains can give rise to image contrast due to x-ray (magnetic) linear and circular dichroism.(27) The detection of secondary low kinetic energy electrons in PEEM makes it a surface sensitive method with a probing depth determined by the effective electron escape depth. In case of iron oxide bulk, the escape depth of secondary electrons at the Fe L3,2 absorption edge is about 5 nm.(40) Hence, the majority of the iron oxide nanocrystals (10 nm average diameter) contributes to the PEEM signal and the spectra do not only reflect contributions from the particle surface. The best lateral spatial resolution achieved by PEEM to date is about 20 nm, but it depends strongly, in addition to the settings of the instruments, on the topography and conductivity of the sample. In the studies presented here, the spatial resolution was about 150 nm. The spherical grating monochromator of the beamline provides monochromatic X-rays with an energy resolution of E/DE ~1800 in the energy range of 250 - 1200 eV. However, in order to improve the signal to noise ratio in this study the beamline was optimized for high flux rather than for energy resolution, which was approximately E/?E = 800 at a photon flux of about 1012 photon/s in the illuminated spot of (30 μm)2.

The nature of PEEM microscopy demands that the sample fulfills certain requirements to enable spatially resolved soft x-ray absorption spectroscopy on a sub-micron length scale. For instance, the high electric field between the sample and the microscope objective lens requires that the sample is planar and has sub-micron surface roughness over a millimeter length scale to reduce electric field inhomogeneity. In addition, the substrate should preferably have a finite conductivity to reduce the amount of electrostatic charging, which causes image drifts and can lead to sudden discharges potentially damaging the sample. For the measurement of the x-ray absorption of individual nanometer-sized nanocrystals, it is further required to

disperse the nanocrystals on the substrate ensuring that the average nearest neighbor distance is significantly larger than the spatial resolution limit of the PEEM microscope. Of particular importance for this experiment is that the contribution of the substrate to the secondary photoelectron signal is as low as possible to enhance the contrast at the Fe L3,2 absorption edge of the g-Fe2O3 nanocrystals with 10 nm in diameter, which corresponds to only about 20,000 iron atoms.

In initial attempts to minimize background contributions we used 400 mesh Copper grids covered with an ultrathin Carbon film (2 - 3 nm thickness), which are often employed for TEM studies of nanocrystals. However, since the films are not planar and are also mechanically unstable, it proved difficult to achieve good imaging conditions. Difficulties were also encountered with other thin film substrates like Si3N4 membranes, which showed pronounced charging effects. A subsequent extensive survey of several potential substrate candidates showed that freshly cleaved highly oriented pyrolytic graphite (HOPG) as well as HF-etched silicon wafers represented the best compromise fulfilling the above-mentioned requirements.

Since the secondary electron yield signal at the Fe L3,2 absorption edge was found to be smaller for HOPG than Silicon wafers, HOPG is, in principle, the better substrate to achieve a low background contribution from the substrate. However, it proved difficult to disperse individual, well-separated g-Fe2O3 nanocrystals from organic solvents onto HOPG. In fact, high-resolution SEM images showed that during deposition the nanocrystals always agglomerated into small islands of 4 - 30 particles.(41) In contrast, the use of HF-etched silicon wafers as substrates allowed dispersing reproducibly individual and well-separated g-Fe2O3 nanocrystals. The main factors influencing the coverage and mean nearest particle distance were, as expected, the particle concentration in the solvent as well as the amount of liquid deposited.

To determine the average particle coverage we have recorded 17 low-magnification SEM images like the one shown in Fig. 1A) with a total area of 320 mm2 and a total of 377 particles. The coverage per image varied from 0.5 particles / mm2 to 2.1 particles / mm2, giving an overall average coverage of 1.2 particles / mm2 with a standard deviation of 0.4 particles / mm2. From the relative positions of the particles in the SEM images, a mean first nearest neighbor distance of 485 nm was derived. This is sufficiently larger than the spatial resolution of 150 nm of the PEEM microscope in this study. However, we note that about 13% and 2% of all particles have a first and second nearest neighbor distance smaller than 150 nm. In consequence, about 13% of the objects showing contrast in PEEM images at the Fe L3,2 absorption edges might be due to the x-ray absorption of "dimers" and "trimers" of particles and not single nanocrystals.

PEEM images were recorded for 80 sec at the same location on the sample described above. Since the detection system of the PEEM (CCD camera and Phosphor screen) has a spatially varying dark count rate and sensitivity the raw images need to be corrected by subtraction of a dark image Dt and division by a sensitivity image St'.42 The dark image Dt is acquired without x-ray illumination using the same exposure time t used for the raw image. Illuminating the phosphor screen homogeneously by defocusing the microscope and subtracting the dark image generates the sensitivity image St'. The exposure time t' of the sensitivity image differs from t because the detector sensitivity variation is not directly a function of the exposure time but of the electron flux per time which reaches the detector. Dark and

sensitivity images can be reused and only have to measured once because the detector sensitivity is constant in time. Only for better visualization the image contrast is enhanced by a factor of 2-8 and the image is subjected to a median filter. For recording of the images, the photon energy was selected to match the Fe L3 absorption edge at 707 eV (Fig. 2A) and at 696 eV to be just below the absorption edge (Fig. 2B). Hence, while the atoms of the iron oxide nanocrystals and of the substrate contribute in a comparable way to the image shown in Fig. 2B), the signal of the nanocrystals is amplified in Fig. 2A) due to the resonant excitation of the iron atoms at 707 eV. Comparing the two images, one notices faint bright spots covering the surface in Fig. 2A), which are absent in the PEEM image in Fig. 2B). Bearing in mind the resonant iron contribution to the image in Fig. 2A), one concludes that these faint spots are due to the absorption of x-rays by iron oxide nanocrystals. Subtracting the pre-edge excited image from the resonantly excited image further enhances the contribution of the iron oxide nanocrystals to the PEEM image. This procedure increases the elemental contrast, suppresses the contribution from any topographic contrast and corrects for illumination inhomogeneities. The resulting PEEM contrast image shown in Fig. 2C) displays bright spots associated with the absorption of iron atoms. PEEM control experiments using HF-etched silicon wafers on which no iron oxide nanocrystals have been deposited did not show any indication of the presence of iron atoms on the surface. Therefore, it can be concluded that the bright spots observed at the Fe L3-edge in the PEEM contrast image in Fig. 2C) are indeed related to the presence of iron oxide nanocrystals. The varying brightness of the spots in the contrast image in Fig. 2C) is most likely related to the rather broad size distribution of the iron oxide nanocrystals in the sample with an average diameter and a standard deviation of 10 nm and 3 nm, respectively. Unfortunately, the limited signal-to-noise ratio prevents a thorough statistical analysis of the spot intensitites and subsequent comparison with the particle size distribution as determined by TEM.

While the distribution and density of bright spots in the PEEM contrast image in Fig. 2C) looks similar to the low-magnification SEM image in Fig. 1A), a detailed analysis of 7 PEEM images with a total area of 1226 mm2 and 743 particles gives a slightly different result for the average substrate coverage. As expected from the lower spatial resolution of PEEM, the smallest nearest neighbor distance detected with PEEM is only 164 nm, in comparison to a minimum distance of 27 nm according to SEM. More significantly, however, the particle coverage according to PEEM varies between images from 0.5 particles / mm2 to 0.8 particles / mm2, which yields a statistically average coverage of 0.6 particles/mm2 with a standard deviation of 0.1 particles / mm2 between different PEEM images. This compares to a coverage of (1.2 ± 0.4) particles / mm2 as determined by SEM.

This apparent discrepancy can be easily explained since many possible sources for systematic uncertainties have to be considered. First, since the total area analyzed by PEEM is about 4 times larger than in case of SEM, a non-uniform particle distribution on the silicon wafer has a bigger influence on the statistical analysis of SEM images. This can be seen, for instance, in the bigger standard deviation of the particle density of 30% as determined by SEM compared to 17% with PEEM between different images. A related aspect is the smaller field of view of SEM at the magnification at which the nanocrystals are still discernible on the surface. Since SEM always requires some surface topography to focus the image, empty areas with no or very small numbers of nanocrystals arising from a non-uniform deposition were not recorded, thereby falsifying the analysis of the

particle coverage by SEM. In addition, while all the features in the PEEM contrast image in Fig. 2C) are related to the presence of iron oxide nanocrystals on the silicon wafer, this cannot be guaranteed for the features in low-magnification SEM images. While care was taken to prepare clean HF-etched silicon wafers, it is possible that some features in the SEM images are actually topographic variations on the silicon wafer or residues from the etching/cleaning process. In consequence, counting such features in SEM images falsely as iron oxide nanocrystals will yield an average particle coverage that is too high compared to the particle density as determined by PEEM. On the other hand, the possibility cannot be excluded that the current PEEM microscope is not sensitive enough to detect all particles on the substrate. Specifically, PEEM might be unable to detect the smallest particles within the size distribution since the amount of absorbing iron atoms, and in consequence the number of emitted secondary photoelectrons, is too small. These questions can be addressed experimentally by using samples with differing average particle sizes but very narrow size distributions (<5%) as well as the use of alignment markers on the substrate which will allow to investigate the very same sample area in SEM or TEM and PEEM. Experiments addressing these issues are currently planned.

To measure spatially resolved x-ray absorption spectra, a series of PEEM images like the ones in Fig. 2A) was recorded for a series of x-ray photon energies around the Fe L3,2 absorption edges with an acquisition time of 15 sec per energy point (20 min. total). The images were processed as described above and a small image drift of about 5 pixel (1 pixel = 20 nm) due to sample charging effects was corrected. To obtain spatially resolved x-ray absorption spectra of single g-Fe2O3 nanocrystals, the intensity in a circular area with 8 pixels diameter, centered on the bright spots in the PEEM contrast image (Fig. 2C), was integrated. This procedure ensures that noise from the background is minimized and it is effectively analogous to minimizing the excitation/detection sample volume in single molecule spectroscopy by using confocal microscopy techniques. To correct for beam intensity variations, background spectra were calculated in a similar fashion from areas close to the bright spots and used for normalization. In Fig. 3A), the local x-ray absorption spectra of a location appearing bright in Fig 2C) (area I) is compared to the one of a dark area (area II). As expected, the spectrum of the bright spot (area I) shows the signature of the Fe L3 absorption edge at 707 eV, whereas the dark background (area II) shows no detectable structure of the absorption intensity in this energy range. Due to the moderate energy resolution, the multiplet structure of the typical x-ray absorption spectra of Fe3+-ions at the L3-edge is not resolved. We note that in case of Fig. 3A), the absorption of the Fe3+-ions at the L2-edge still can be clearly distinguished from the background. In Fig. 3B), the x-ray absorption spectra of several positions with varying intensities in Fig. 2C) (areas III - VII) are compared. Clearly, even in cases with very small intensity in the contrast image in Fig. 2C) the Fe L3 x-ray absorption edge is still discernible from the background whereas the weaker L2 edge is barely recognizable. We emphasize that these spectra indeed reflect the x-ray absorption spectra of individual particles with diameters of (10 ± 3) nm with a small chance that some spectra are due to the presence of dimers or trimers of particles (< 13%). To the best of our knowledge, this represents the first time that soft x-ray absorption spectra of individual nanocrystals at this length scale are reported.(37)

As mentioned above, the varying intensity of the L3 x-ray absorption edges in Fig. 3) reflects the varying numbers of Fe-atoms in the particles due to the broad particle size distribution. Obviously, this information can, in

principle, be used to correlate properties measured by x-ray absorption spectroscopy with the size of the individual particle under investigation. Furthermore, in case of binary core-shell or alloy nanoparticles the relative intensity of the x-ray absorption edges of the two elements should allow determining the relative ratios of the two elements in individual particles. Such an element-mapping experiment would require only measuring contrast images at the two absorption edges thereby allowing a quick assessment about how much the chemical composition varies from particle to particle in the sample.

Fig. 4A) shows a comparison of the x-ray absorption spectrum of an individual iron oxide nanocrystal ("single") with the spectrum obtained by averaging over many single particle spectra ("average") as well as with the integral, non-spatially resolved spectrum obtained by integrating the whole area of the contrast image in Fig. 2C) ("ensemble"). Obviously, within the spectral resolution of the experiment no significant difference can be observed. In addition, conventional high-resolution soft x-ray absorption spectroscopy of g-Fe2O3 nanocrystal powders with average particle sizes from 4 nm to 13 nm recorded at beamline 10-1 at the Stanford Synchrotron Radiation Source (SSRL) showed essentially the same absorption features as g-Fe2O3 bulk (see Fig. 4B)). The localized and atomic-like nature of the resonant transition at the Fe L3,2 absorption edge43 is responsible for this observation which makes it unlikely to observe size-dependent changes as a result of surface reconstructions or finite-size effects in small g-Fe2O3 particles. This is unlike the case of colloidal CdSe and InAs nanocrystals with a more delocalized electronic band structure where a strong broadening of the soft x-ray absorption spectra at the Cd and In M5,4 edges was observed with decreasing particle size.31 Multiple-scattering calculations indicated that the broadening might be due to structural disorder in the CdSe and InAs particles induced by surface reconstructions. Unfortunately, the very weak Cd and In M5,4 edges do not allow the study of individual CdSe and InAs nanocrystals with the current PEEM instrument.

An important finding of our study is the fact that the g-Fe2O3 core of the nanocrystals is apparently stable enough to withstand repeated exposure to an intense x-ray beam. Neither several contrast images nor x-ray absorption spectra recorded of the same sample area with about 1 hour of continuous exposure to the x-ray beam between them revealed any differences. While we expect radiation induced damages to the organic surfactant shell, our observation at the Fe L3 edge illustrates that effects like excessive charge accumulation on the particles potentially causing a Coulomb explosion or the particles becoming buried in a thick and dense, amorphous carbon layer via radiation-induced damages of the organic surfactant shell are not significant. This is in stark contrast to EELS studies that are often complicated by sample decomposition in the strong and intensely interacting electron beam limiting the exposure time significantly and, thereby, the possible signal-to-noise ratio of EELS spectra.

In addition, the sensitivity of x-ray absorption spectroscopy to magnetic properties makes PEEM a potentially unique tool for investigating individual nanocrystals of magnetic materials. In particular, the current developments of aberration corrected PEEMs (SMART at Bessy, Berlin44 and PEEM3 at ALS, Berkeley(45) should improve the detection efficiency (currently only about 5% of all secondary photoelectrons generated are detected at PEEM2) to an extent that time resolved experiments like the study of magnetic reversal or temperature induced solid-solid state phase transitions of individual nanocrystals might become possible. In addition, the improved performance

will allow increasing the spatial resolution to about 2 nm enabling spatially resolved x-ray imaging and spectroscopy comparable to current state-of-the-art EELS instruments while maintaining the generally better spectral resolution of x-ray spectroscopy.

Summary

In summary, the application of x-ray spectromicroscopy to the study of the Fe L3,2 edge soft x-ray absorption of single g-Fe2O3 nanocrystals with 10 nm average diameter has been demonstrated using resonantly excited x-ray photoemission electron microscopy. The particles do not degrade even after prolonged exposure to the intense x-ray beam. We observe strong intensity variations in the PEEM contrast images and the absorption edges between individual particles reflecting the size distribution of the sample. However, no differences with respect to the position or shape of the spectrum of an individual particle and the ensemble can be observed within the moderate energy resolution of the experiment. High-resolution soft x-ray experiments of ensembles of g-Fe2O3 bulk and nanocrystals with sizes ranging from 4 nm to 13 nm confirmed the size-independence of the spectral features, which is in accordance with the spatially very localized wave functions of the electronic states involved in the x-ray absorption process in iron oxide.

Fig. 1A) Low-magnification SEM image of g-Fe2O3 nanocrystals deposited onto HF-etched Silicon wafer. The average particle coverage determined from 17 similar images is (1.2 ± 0.4) part. / mm2 with an average interparticle distance of 485 nm.
Fig. 1B) High-magnification SEM image of the sample shown in Fig. 1A). The bright spots show no evidence of consisting of agglomerates of nanocrystals. In addition, the FWHM of line-scans through these spots range typically from 8 - 15 nm, which is in good agreement with the particle size of (10 ± 3) nm of individual g-Fe2O3 nanocrystals as determined by TEM.
Fig. 2A) Resonantly excited PEEM image of g-Fe2O3 nanocrystals on HF-etched Silicon wafer using a photon energy matching the iron L3 absorption edge (707 eV).
Fig. 2B) PEEM image of the same spot as in Fig. 2A), but recorded with a x-ray photon energy of 696 eV right before the Fe L3 absorption edge.
Fig. 2C) PEEM contrast image obtained by subtracting the image in Fig. 2B) from the one in Fig. 2A). This procedure eliminates the energy-independent background in the image and emphasizes contrast due to the x-ray absorption by iron atoms.
Fig. 3A) Spatially resolved X-ray absorption spectra at the Fe L3,2 absorption edge. The secondary photoelectron signal is plotted as a function of the incident x-ray energy for two selected areas I and II in Fig. 2C). As expected, the spectra of the bright spot (area I) in Fig. 2C) shows a strong increase of signal intensity at the Fe L3 absorption edge whereas the spectra of the dark spot (area II) remains flat.
Fig. 3B) Spatially resolved X-ray absorption spectra at the Fe L3,2 absorption edge of different regions (III - VII) with varying brightness in the PEEM contrast image of Fig. 2C). The variable intensity at the Fe L3 absorption edge is due to the varying size of the individual g-Fe2O3 nanocrystals.
Fig. 4A) Comparison of the spatially resolved Fe L3,2 X-ray absorption edge spectrum of a single iron oxide nanocrystals ("single"), the spectrum obtained by averaging over all spatially resolved single nanocrystal x-ray absorption spectra ("average") and the integral, non-spatially resolved

intensity ("ensemble") in the PEEM contrast image in Fig. 2C). Within the moderate energy resolution of the experiment (~1 eV), the spectra appear to be identical.

Fig. 4B) Conventional ensemble x-ray absorption spectra at the Fe L3,2 absorption edge of g-Fe2O3 bulk and nanocrystals measured with high resolution (~ 0.3 eV) at beamline 10.1 of the Stanford Synchrotron Radiation Laboratory, Stanford. No significant size-dependent changes between bulk and the nanocrystals can be observed. Please note, that for clarity only every 4th data point is displayed.

1 A. P. Alivisatos, P. F. Barbara, A. W. Castleman, J. Chang, D. A. Dixon, M. L. Klein, G. L. McLendon, J. S. Miller, M. A. Ratner, P. J. Rossky, S. I. Stupp, and M. E. Thompson, Adv. Mater. 10, 1297-1336 (1998).

2 National Science and Technology Council, (2000).

3 X. Peng, J. Wickham, and A. P. Alivisatos, J. Am. Chem. Soc. 120, 5343 (1998).

4 L. Manna, E. C. Scher, and A. P. Alivisatos, J. Am. Chem. Soc. 122, 12700 - 12706 (2000).

5 C. B. Murray, C. R. Kagan, and M. G. Bawendi, Ann. Rev. Mat. Science 30, 545 (2000).

6 D. V. Talapin, S. Haubold, A. L. Rogach, A. Kornowski, M. Haase, and H. Weller, J. Phys. Chem. B 105, 2260 (2001).

7 C. B. Murray, S. Sun, W. Gaschler, H. Doyle, T. A. Betley, and C. R. Kagan, IBM J. Res. & Dev. 45, 47 (2001).

8 V. F. Puntes, K. M. Krishnan, and A. P. Alivisatos, Science 291, 2115-2117 (2001).

9 Y.-W. Jun, S.-M. Lee, N.-J. Kang, and J. Cheon, J. Am. Chem. Soc. 123, 5150 (2001).

10 L. Qu, Z. A. Peng, and X. Peng, NanoLett. 1, 333 (2001).

11 S. Empedocles, R. Neuhauser, K. Shimizu, and M. G. Bawendi, Adv. Mater. 11, 1243 (1999).

12 J. T. Hu, L. S. Li, W. D. Yang, L. Manna, L. W. Wang, and A. P. Alivisatos, Science 292, 2060-2063 (2001).

13 A. Mews, F. Koberling, T. Basche, G. Philipp, G. S. Duesberg, S. Roth, and M. Burghard, Adv. Mater. 12, 1210 (2000).

14 A. Jorio, R. Saito, J. H. Hafner, C. M. Lieber, M. Hunter, T. McClure, G. Dresselhaus, and M. S. Dresselhaus, Phys. Rev. Lett. 86, 1118-21 (2001).

15 U. Banin, Y. W. Cao, D. Katz, and O. Millo, Nature 400, 542 (1999).

16 T. W. Tombler, C. W. Zhou, L. Alexseyev, L. Kong, H. J. Dai, L. Lei, C. S. Jayanthi, M. J. Tang, and S. Y. Wu, Nature 405, 769 (2000).

17 T. W. Odom, J. H. Hafner, and C. M. Lieber, Top. Appl. Phys. 80, 173 (2001).

18 A. Mews, A. V. Kadavanich, U. Banin, and A. P. Alivisatos, Phys. Rev. B 53, 13242 (1996).

19 X. Peng, M. C. Schlamp, A. V. Kadavanich, and A. P. Alivisatos, J. Am. Chem. Soc. 119, 7019 (1997).

20 Z. L. Wang, J. Phys. Chem. B 104, 1153 (2000).

21 Z. L. Wang, Z. R. Dai, and S. H. Sun, Adv. Mater. 12, 1944 (2000).

22 O. Stephan, A. Gloter, D. Imhoff, M. Kociak, C. Mory, K. Sunega, M. Tence, and C. Colliex, Surf. Rev. Lett. 7, 475 (2000).

23 O. Stephan, M. Kociak, L. Henrard, K. Sunega, A. Gloter, M. Tence, E. Sandre, and C. Colliex, J. Electron Spectrosc. 114, 209 (2001).

24 A. V. Kadavanich, T. C. Kippeny, M. M. Erwin, S. J. Pennycook, and S. J. Rosenthal, J. Phys. Chem. B 105, 361 (2001).

25 S. A. Majetich and Y. Jin, Science 284, 470 (1999).

26 X-ray Absorption: Principles, Applications, Techniques of EXAFS, SEXAFS and XANES, Vol., edited by D. C. Koningsberger and R. Prins (Wiley, New York, 1988).
27 J. Stöhr, NEXAFS Spectroscopy (Springer, New York, 1992).
28 J. Rockenberger, L. Tröger, A. Kornowski, T. Vossmeyer, A. Eychmüller, J. Feldhaus, and H. Weller, J. Phys. Chem. B 101, 2691 (1997).
29 J. Rockenberger, L. Tröger, A. Rogach, M. Tischer, M. Grundmann, A. Eychmüller, and H. Weller, J. Chem. Phys. 108, 7807 (1998).
30 J. Lüning, J. Rockenberger, S. Eisebitt, J.-E. Rubensson, A. Karl, A. Kornowski, H. Weller, and W. Eberhardt, Solid State Comm. 112, 5 (1999).
31 K. S. Hamad, R. Roth, J. Rockenberger, T. v. Buuren, and A. P. Alivisatos, Phys. Rev. Lett. 83, 3474 (1999).
32 T. Warwick, H. Ade, A. P. Hitchcock, H. Padmore, E. G. Rightor, and B. P. Tonner, J. Electron Spectrosc. 84, 85 (1997).
33 M. Kiskinova, Surf. Rev. Lett. 7, 447-453 (1999).
34 J. Stöhr and S. Anders, IBM J. Res. & Dev. 44, 535 (2000).
35 A. P. Hitchcock, J. Synchr. Radiat. 8, 66 (2001).
36 S. Heun, Y. Watanabe, B. Ressel, D. Bottomley, T. Schmidt, and K. C. Prince, Phys. Rev. B 63, 125335 (2001).
37 Note, that the photoemission spectra of "individual" InAs nanocrystals reported by Heun et al., Phys. Rev. B 2001, 63, 125335, represent averages over all InAs nanocrystals imaged. Also, the InAs nanocrystals with an average diameter and height of 55 nm and 22 nm, respectively, contain significantly more atoms (factor of 40) than the 10 nm g-Fe2O3 nanoparticles investigated here.
38 J. Rockenberger, E. C. Scher, and A. P. Alivisatos, J. Am. Chem. Soc. 121, 11596 (1999).
39 S. Anders, H. A. Padmore, R. M. Duarte, T. Renner, T. Stammler, A. Scholl, M. R. Scheinfein, J. Stöhr, L. Séve, and B. Sinkovic, Rev. Sci. Instr. 70, 3973 (1999).
40 S. Gota, M. Gautier-Soyer, and M. Sacchi, Phys. Rev. B 62, 4187 (2000).
41 F. Nolting, J. Lüning, J. Rockenberger, J. Hu, and A. P. Alivisatos, submitted.
42 A. Scholl, H. Ohldag, F. Nolting, J. Stöhr, and H. A. Padmore, to be published in Rev. Sci. Instrum. (2001).
43 P. Kuiper, B. G. Searle, P. Rudolf, L. H. Tjeng, and C. T. Chen, Phys. Rev. Lett. 70, 1549 (1993).
44 R. Fink, M. R. Weiss, E. Umbach, D. Preikszas, H. Rose, R. Spehr, P. Hartel, W. Engel, R. Degenhardt, R. Wichtendahl, H. Kuhlenbeck, W. Erlebach, K. Ihmann, R. Schlogl, H. J. Freund, A. M. Bradshaw, G. Lilienkamp, T. Schmidt, E. Bauer, and G. Benner, J. Electron Spectrosc. 84, 231 (1997).
45 J. Feng, H. Padmore, D. H. Wei, S. Anders, Y. Wu, A. Scholl, and D. Robin, to be published in Rev. Sci. Instrum. (2001).

Personnel Supported:

Principal Investigator: Paul Alivisatos
Postdoctoral Researcher: Joerg Rockenberger
Graduate Students: David Zaziski, Liang-shi Li, Stephen Prilliman, Kim Hamad

Publications:

Joerg Rockenberger, Erik C. Scher, A. Paul Alivisatos, "A New Non-Hydrolytic Single-Precursor Approach to Surfactant-Capped Nanocrystals of Transition Metal Oxides," J. Am. Chem. Soc., **121**, N49, 11595-11596 (December 1999).

Joerg Rockenberger, Frithjof Nolting, Jan Luening, Jiangtao Hu, and A. Paul Alivisatos, "Soft X-ray Imaging and Spectroscopy of Single Nanocrystals," in press, J. Chem. Phys.

Kimberly Hamad, "X-Ray and Photoelectron Spectroscopy of the Structure, Reactivity, and Electronic Structure of Semiconductor Nanocrystals," University of California, Berkeley, Ph.D. Thesis, Spring 2000.

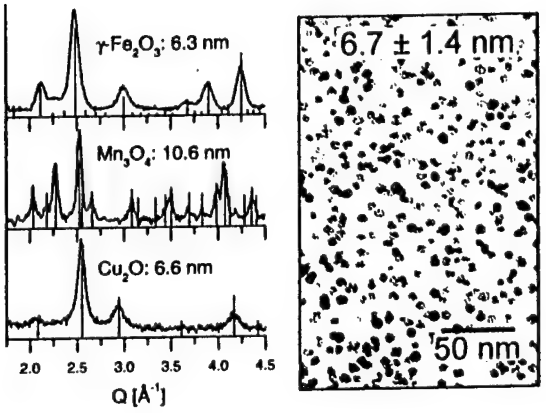
γ-Fe2O3: 6.3 nm
Mn3O4: 10.6 nm
Cu2O: 6.6 nm
2.0
2.5
3.0
3.5
4.0
4.5
Q [Å-1]
6.7 ± 1.4 nm
50 nm

Fig. 1

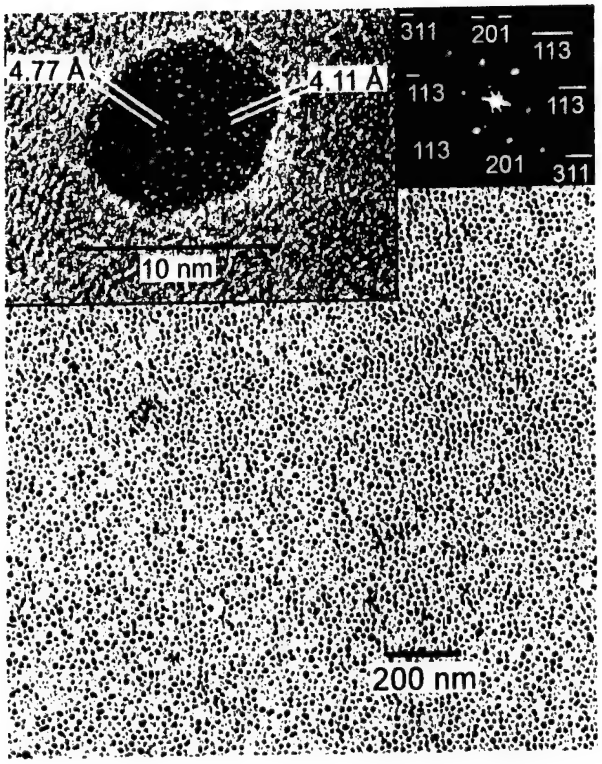

Fig. 2

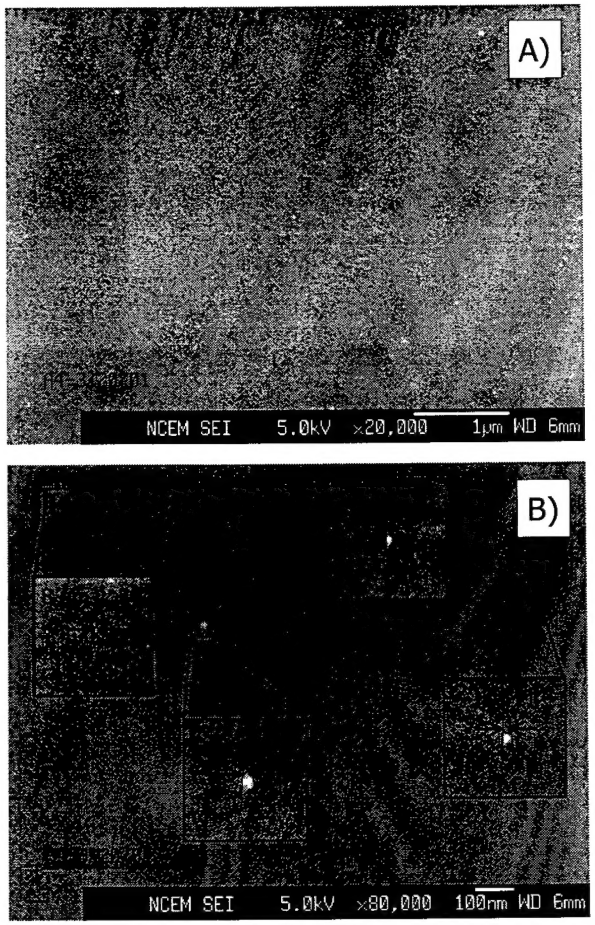

Figure 1, Rockenberger et al., J. Chemical Physics

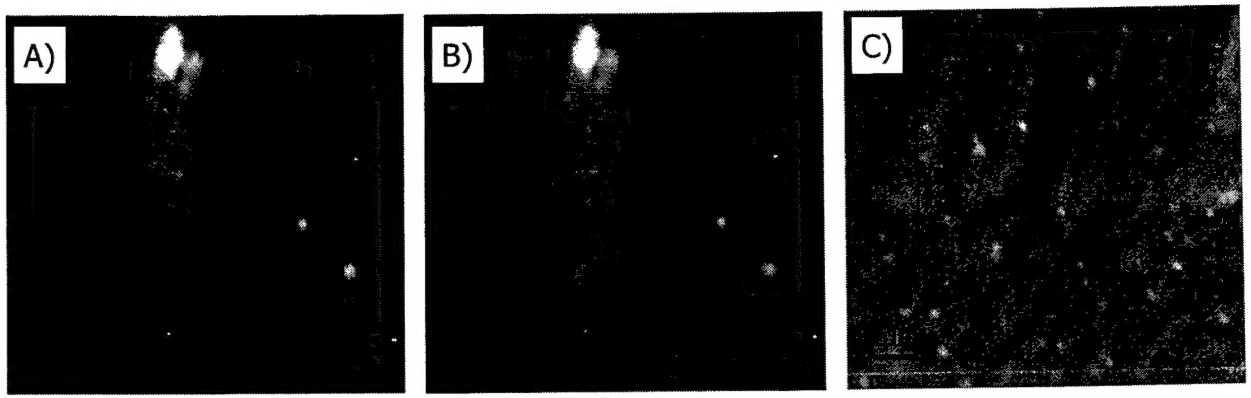

Figure 2, Rockenberger et al., J. Chemical Physics

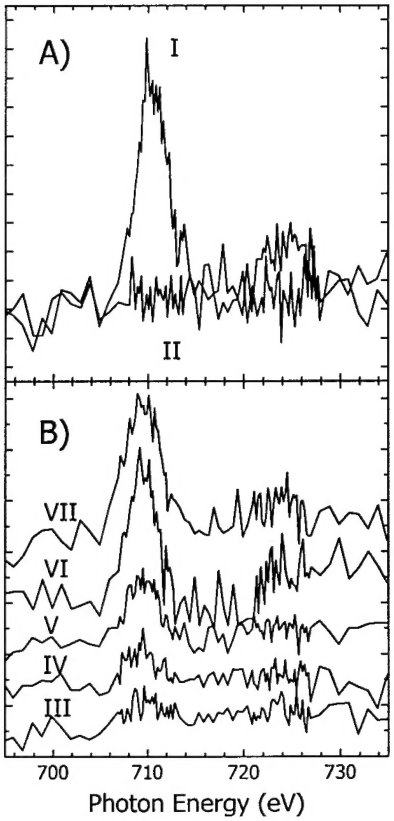

Figure 3, Rockenberger et al., J. Chemical Physics

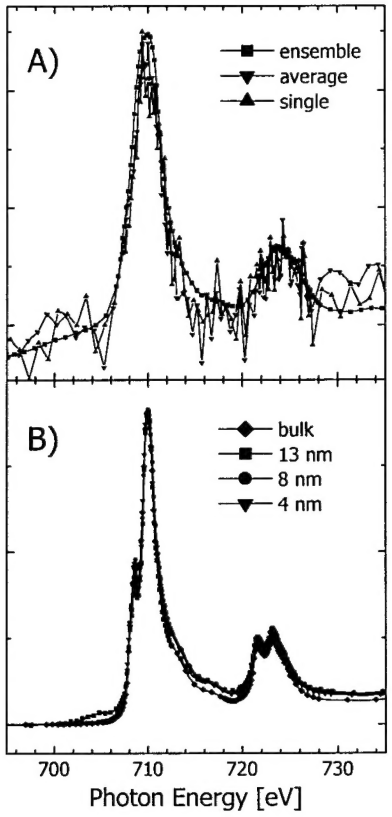

Figure 4, Rockenberger et al., J. Chemical Physics